

Key Points:

- Passing atmospheric cold fronts generate a large area of growing wind-waves that are misaligned with local wind
- Parameterized effect of misaligned waves increases the roughness length, drag and enthalpy coefficients, and wind stress
- Representation of the misaligned wave effect in the bulk formula improves the momentum flux estimates

Correspondence to:

C. Sauvage,
csauvage@whoi.edu

Citation:

Sauvage, C., Seo, H., Barr, B. W., Edson, J. B., & Clayton, C. A. (2024). Misaligned wind-waves behind atmospheric cold fronts. *Journal of Geophysical Research: Oceans*, 129, e2024JC021162. <https://doi.org/10.1029/2024JC021162>

Received 6 APR 2024

Accepted 5 AUG 2024

Author Contributions:

Conceptualization: César Sauvage, Hyodae Seo
Data curation: James B. Edson
Formal analysis: César Sauvage, Hyodae Seo
Funding acquisition: Hyodae Seo, James B. Edson, Carol Anne Clayton
Investigation: César Sauvage, Hyodae Seo
Methodology: César Sauvage, Hyodae Seo
Supervision: Hyodae Seo, James B. Edson, Carol Anne Clayton
Validation: César Sauvage, Hyodae Seo
Visualization: César Sauvage
Writing – original draft: César Sauvage, Hyodae Seo
Writing – review & editing: César Sauvage, Hyodae Seo, Benjamin W. Barr, James B. Edson, Carol Anne Clayton

Misaligned Wind-Waves Behind Atmospheric Cold Fronts

César Sauvage¹ , Hyodae Seo^{1,2} , Benjamin W. Barr¹, James B. Edson¹ , and Carol Anne Clayton¹ 

¹Woods Hole Oceanographic Institution, Woods Hole, MA, USA, ²University of Hawai'i at Mānoa, Honolulu, HI, USA

Abstract Atmospheric fronts embedded in extratropical cyclones are high-impact weather phenomena, contributing significantly to mid-latitude winter precipitation. The three vital characteristics of the atmospheric fronts, high wind speeds, abrupt change in wind direction, and rapid translation, force the induced surface waves to be misaligned with winds exclusively behind the cold fronts. The effects of the misaligned waves under atmospheric cold fronts on air-sea fluxes remain undocumented. Using the multi-year in situ near-surface observations and direct covariance flux measurements from the Pioneer Array off the coast of New England, we find that the majority of the passing cold fronts generate misaligned waves behind the cold front. Once generated, the waves remain misaligned, on average, for about 8 hr. The parameterized effect of misaligned waves in a fully coupled model significantly increases the roughness length (185%), drag coefficient (19%), and air-sea momentum flux (11%). The increased surface drag reduces the wind speeds in the surface layer. The upward turbulent heat flux is weakly decreased by the misaligned waves because of the decrease in temperature and humidity scaling parameters being greater than the increase in friction velocity. The misaligned wave effect is not accurately represented in a commonly used wave-based bulk flux algorithm. Yet, considering this effect in the current formulation improves the overall accuracy of parameterized momentum flux estimates. The results imply that better representing a directional wind-wave coupling in the bulk formula of the numerical models may help improve the air-sea interaction simulations under the passing atmospheric fronts in the mid-latitudes.

Plain Language Summary Atmospheric fronts are recurrent weather phenomena in mid-latitudes, significantly contributing to winter precipitation. They are characterized by high wind speeds, abrupt changes in wind direction, and rapid translation. The passage of the fronts over the ocean can generate strongly misaligned waves with the local wind, particularly behind the cold fronts. The effects of these misaligned waves under atmospheric cold fronts on air-sea fluxes remain undocumented. Using the long-term surface observations from the Pioneer Array off the coast of New England, we find that the majority of the passing atmospheric fronts generate misaligned waves behind the cold front, which can remain misaligned, on average, for about 8 hr. By increasing the ocean roughness length in case of misaligned waves in coupled numerical experiments, a significant increase in momentum flux is found, which reduces the surface wind speeds. The misaligned wave effect is not accurately represented in a commonly used wave-based air-sea flux algorithm. Yet, by considering this effect in the current formulation, the overall accuracy of parameterized momentum flux estimates is improved. A better representation of the air-sea interaction in numerical models is crucial for a better understanding of regional and global climate.

1. Introduction

Air-sea momentum, heat, and moisture exchanges are mediated by interactions between near-surface atmospheric turbulence and the ocean surface wavefield. Wave fields are complex and may include contributions from a wide range of frequencies and directions. This includes strongly coupled short wind-waves with wavelengths of $O(0.1\text{--}10\text{ m})$ and frequencies exceeding twice the spectral peak (Kukulka & Hara, 2005; Makin et al., 1995; Phillips, 1966), developing and mature locally generated wind-waves and remotely generated long-period swell. In many current modern sea state-dependent (or wave-based) bulk flux algorithms, the surface waves that determine the surface drag are often assumed to be in the direction of winds. However, there are many wind and wave regimes where this assumption is not valid and where using it can yield notable deficiencies in the parameterized momentum flux. Swell waves under the low-wind condition (G. Chen et al., 2002; Grachev & Fairall, 2001; Hanley & Belcher, 2008; Hanley et al., 2010; Sullivan et al., 2008) or the mixed seas under the trade wind (Sauvage et al., 2023) or tropical cyclones (S. S. Chen & Curcic, 2016; S. S. Chen et al., 2013; X. Chen et al., 2020; Hsu et al., 2019; Reichl et al., 2014) are well-known examples in the lower-latitudes. Existing studies

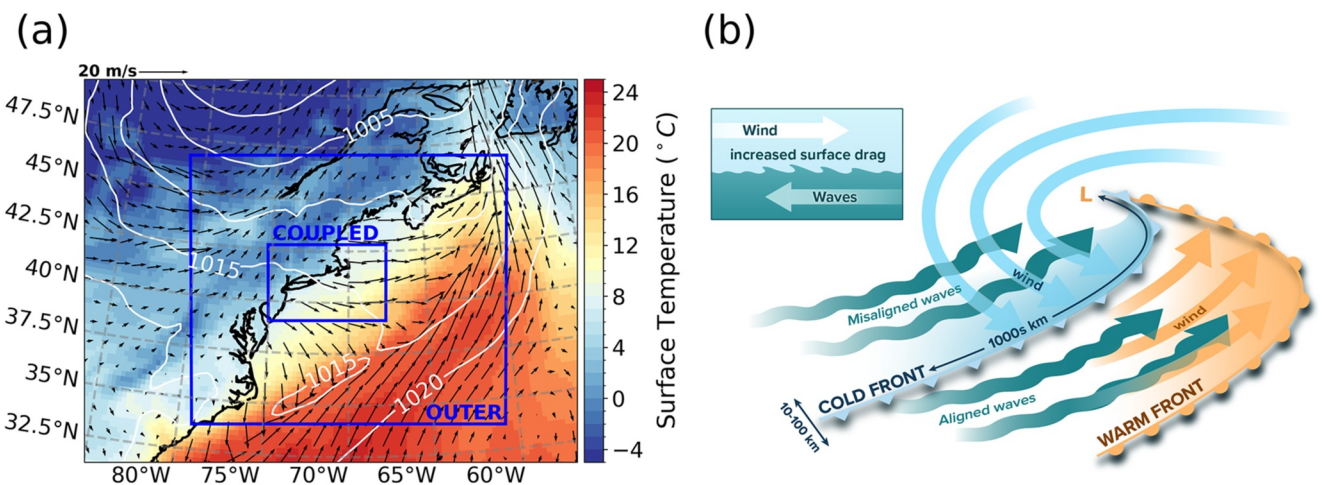


Figure 1. (a) An extratropical cyclone in the North Atlantic on 7 December 2017, at 00:00 UTC, showing the surface air temperature ($^{\circ}\text{C}$), overlaid with the mean sea level pressure (contours, hPa) and the surface wind (arrows), from the ERA5 reanalysis. The extent of the outer and nested model domains is also indicated. (b) A schematic representation of an atmospheric front passing over the ocean showing aligned wind-waves under the warm sector and strongly misaligned waves behind the cold front. The schematic at the top left represents the mechanism of the enhanced drag behind the cold front when wind and waves are misaligned. The “L” symbol denotes the center of the low-pressure system.

suggest a complex relationship between wind-wave misalignment and surface stress, which may be regime-dependent (e.g., high winds in tropical cyclones vs. lower winds in mid-latitudes). For instance, Zhou et al. (2022) found that misalignment between local winds and tropical cyclone-generated swell reduced the drag coefficient in high winds, suggesting quadrant-specific variations in drag due to storm-scale misalignment patterns. In contrast, Patton et al. (2019) and Porchetta et al. (2019, 2021) examined in situ observations from the North Sea and the U.S. New England coast and found that wind-wave misalignment increases the surface drag, with additional influence by wave age.

In the mid-latitudes, the atmospheric fronts are embedded in the extratropical cyclones and significantly modulate the day-to-day weather variability. They feature elongated along-frontal scales of 1,000s km comparable to the lateral extent of the extratropical cyclones, but much shorter cross-frontal scales of 10–100 km (Figure 1, Bjerknes & Solberg, 1922). Figure 1a shows a typical extratropical cyclone we will examine in this study. Traveling eastward at $\approx 10 \text{ ms}^{-1}$ the atmospheric fronts accompany gale-force near-surface winds ($15\text{--}30 \text{ ms}^{-1}$), which also abruptly shift in direction from the southerly in the warm sector to the northwesterly in the cold sector. Atmospheric fronts are detected at a given time and location on a certain pressure level. Different studies use different parameters and empirical thresholds. The most well-known is based on the thermal front parameter related to the temperature of the fronts (Renard & Clarke, 1965). Recently, Parfitt et al. (2017) used a combination of normalized vorticity and temperature gradients to diagnose fronts. Although atmospheric fronts are typically detected only 10%–30% in the wintertime North Atlantic (Berry et al., 2011; Hewson, 1998; Parfitt et al., 2017; Reeder et al., 2021), they are known to contribute to up to 90% of the precipitation (Catto & Pfahl, 2013; Soster & Parfitt, 2022), often in an extreme form (Catto & Pfahl, 2013) and, hence, they are one of the most important high-impact weather phenomena in the mid-latitudes. Interactions between the cold airmass of the fronts and the warmer ocean (and ocean fronts) via air-sea turbulent heat fluxes influence the intensity of these events (Parfitt et al., 2016; Seo et al., 2023). The atmospheric cold fronts are also known to force significant surges and complex wave reactions that severely impact coastal and estuary circulations and wetland evolutions (Cao et al., 2020; Guo et al., 2020; Kim et al., 2020). However, their impacts on surface drag and momentum flux in the mid-latitudes are undocumented in the literature. We will demonstrate that directional wave-wind coupling can modulate these surface fluxes, impacting the surface drag and near-surface winds.

The three crucial characteristics of atmospheric fronts are high winds, abrupt changes in wind direction, and the ability to move rapidly across a region. These are particularly relevant for misaligned waves, as the wave fields cannot adjust immediately to the atmospheric variations. In the warm sector of the fronts, the strong southerly winds force the strongly coupled short wind-waves, generally aligned with the winds. Once the cold front is crossed, the marked shift in the wind direction, combined with the rapid eastward translation, generates a large

fetch of growing wind-waves that become quickly misaligned with the northwesterly winds. Figure 1b illustrates this process schematically.

This study identifies and examines the evolutions of misaligned waves under atmospheric fronts using direct in-situ surface flux measurements and fully coupled high-resolution ocean-atmosphere-wave model simulations. A possible modification to more accurately represent the relevant wave-wind physics in the bulk flux parameterization is also discussed. Section 2 describes the observations, parameterizations, and model simulations. Section 3 provides a case study investigation of misaligned waves for one atmospheric front case using model simulations and observations, while Section 4 offers the climatological perspectives of the evolution of misaligned waves and their impacts on parameterized flux using observations. Section 5 concludes the study.

2. Methods

2.1. Observations

The Pioneer Array, located off the coast of New England and operated by the NSF Ocean Observatories Initiative (OOI, NSF Ocean Observatories Initiative, 2023; Trowbridge et al., 2019), provides various meteorological and ocean observations of physical, chemical, and biological processes from December 2014 until November 2022. This study uses the 8-year of near-surface measurements of wind, temperature, humidity, and surface wave fields. In addition, we use the momentum fluxes from the direct covariance flux system (DCFS), available over a shorter period (2015-05-13–2015-10-23; 2016-05-13–2018-03-29; 2018-10-30–2019-04-07). NOAA's National Data Buoy Center (NDBC) buoys off the New England coast are also used, especially surface wave information, including 2D wave spectrum along with significant wave height, dominant wave period, and mean/peak wave direction, co-located with the near-surface measurements of winds, temperature, humidity, pressure, and ocean surface temperature.

2.2. SCOAR Coupled Regional Modeling System

We use the Scripps Coupled Ocean-Atmosphere Regional model (SCOAR, Sauvage et al., 2023; Seo et al., 2007, 2014, 2016, 2021), which couples the Weather Research and Forecast model (WRF, Skamarock et al., 2019) in the atmosphere to the Regional Ocean Modeling System (ROMS, Haidvogel et al., 2000; Shchepetkin & McWilliams, 2005) in the ocean and WAVEWATCH III (WW3, The WAVEWATCH III Development Group, 2019; Tolman et al., 2002) for the surface waves. ROMS is driven by the momentum, heat, and freshwater fluxes parameterized from COARE3.5 (Edson et al., 2013; Fairall et al., 1996, 2003) implemented in the WRF Mellor-Yamada-Nakanishi-Niino (MYNN) surface layer scheme (Jiménez et al., 2012; Nakanishi & Niino, 2009). Specifically for momentum flux, ROMS receives the total stress minus the wave-supported stress and the wave dissipation stress, where the total stress is computed from WRF using the COARE3.5 algorithm, while wave and dissipation stresses are obtained from WW3. ROMS forces WRF by feeding sea surface temperature and surface current vectors to the WRF surface layer scheme. Between WRF and WW3, the model offers various wave-to-atmosphere coupling options to determine the surface fluxes, as documented in detail in Sauvage et al. (2023). This study will examine two particular wave-based roughness length formulations, as described in Section 2.3. To represent the ocean current effects on waves, ROMS provides surface current to WW3. WW3 is also coupled to ROMS to represent energy dissipation due to wave-breaking and whitecapping. The wave-to-ocean energy flux from WW3 is added as a wave dissipation term in the Generic Length Scale (GLS) vertical mixing scheme in ROMS (Warner et al., 2005). In addition, the significant wave height from WW3 is used to scale the GLS background surface roughness length.

2.3. Momentum Flux Parameterizations

The momentum flux (τ), sensible (H_c) and latent (H_l) heat fluxes are parameterized via COARE (Fairall et al., 1996) as:

$$\tau = \rho_a C_D S_r U_r = \rho_a u_*^2, \quad (1)$$

$$H_c = \rho_a C_{pa} C_h S_r \Delta T = -\rho_a C_{pa} u_* T_*, \quad (2)$$

$$H_l = \rho_a L_e C_e S_r \Delta Q = -\rho_a L_e u_* q_*, \quad (3)$$

where ρ_a is the air density, C_{pa} is the specific heat capacity of the air at constant pressure, L_e is the latent heat of evaporation, T is the potential temperature, Q is the water vapor mixing ratio, S_r is the scalar averaged wind speed relative to the ocean surface, U_r is the magnitude of the wind vector relative to the ocean surface, C_D , C_h , C_e are the transfer coefficients for stress, sensible and latent heat, and u_* , T_* , q_* are the Monin-Obukhov similarity scaling parameters. The drag coefficient C_D is defined as:

$$C_D(z, z_0, \psi_m) = \left[\frac{\kappa}{\ln(z/z_0) - \psi_m(\zeta)} \right]^2, \quad (4)$$

where κ is the von Kármán constant, $\psi_m(\zeta)$ is an empirical function of atmospheric stability, ζ is the z/L ratio with L the Obukhov length and z the height above the surface. The COARE wave-based formulation (Edson et al., 2013) parameterizes the wave-induced surface roughness (z_0^{rough} , hereafter simply z_0) as,

$$z_0 = H_s D \left(\frac{u_*}{c_p} \right)^B, \quad (5)$$

where H_s is the significant wave height, u_*/c_p is the inverse wave age based on u_* , and the peak phase speed of the wave (c_p). D and B are numerical constants given by $D = 0.09$ and $B = 2$ (Edson et al., 2013). In addition to Equation 5 included in the COARE3.5 public release, Sauvage et al. (2023) tested a revised formulation, in which z_0 increases as the wave-wind misalignment increases (Porchetta et al., 2019, 2021),

$$z_0 = H_s D \cos(a\theta) \left(\frac{u_*}{c_p} \right)^{B \cos(b\theta)}, \quad (6)$$

where θ is the absolute directional difference between the 10-m wind and the peak wave direction. D and B are the same coefficients as in Equation 5, while the coefficients $a = 0.45$ and $b = -0.32$ are determined by Porchetta et al. (2019) from a set of midlatitude offshore in situ measurements, including the Air-Sea Interaction Tower (ASIT) south of Martha's Vineyard, which is close to the region of the current study.

2.4. Experiments

The model domain covers the North Atlantic (Figure 1a) with a nested configuration. In the outer domain, the model is run at 7.5 km resolution and is atmosphere-only, dynamically downscaling the large-scale atmospheric circulation with spectral nudging. This drives the inner domain zooming over the US Northeast (Figure 1a), where WRF, ROMS, and WW3 are fully coupled at an hourly frequency and run at the identical 1.5 km resolution with matching grids and land-sea masks. ROMS has 30 vertical levels with a stretched vertical grid that enables the enhanced resolutions near the surface and the bottom, with $\theta_s = 7.0$, $\theta_b = 0.1$, and $h_{cline} = 300$ m, yielding a minimum of 15 layers in the upper 150 m. The vertical resolution of WRF is refined to have 50 vertical levels with ≈ 20 levels below 250 m. The lowest level is close to the surface (5.5 m), with the second lowest level at 12 m per Shin et al. (2012).

In WRF, deep cumulus convection is represented through the Multi-scale Kain-Fritsch scheme (Zheng et al., 2016), the cloud micro-physics by the WRF single-moment 6-class scheme (Hong & Lim, 2006), the land surface process by the Noah land surface model (F. Chen & Dudhia, 2001), and the Rapid Radiative Transfer Model for general circulation models (RRTMG, Iacono et al., 2008) for the shortwave and longwave radiations. The planetary boundary layer (PBL) processes are treated with the MYNN level 2.5 scheme (Nakanishi & Niino, 2009). In ROMS, the GLS vertical mixing scheme (Warner et al., 2005) determines vertical eddy viscosity and diffusivity. In WW3, the ST6 package is used to parameterize wind input, wave breaking, and swell dissipation (Babanin, 2011; Liu et al., 2019; Stopa et al., 2016). Nonlinear wave–wave interactions are computed using the discrete interaction approximation (Hasselmann et al., 1985). Reflection by shorelines is enabled through the Arduin and Roland (2012) scheme. The depth-induced breaking is based on Battjes and Janssen (1978), and the bottom friction formulation follows Arduin et al. (2003).

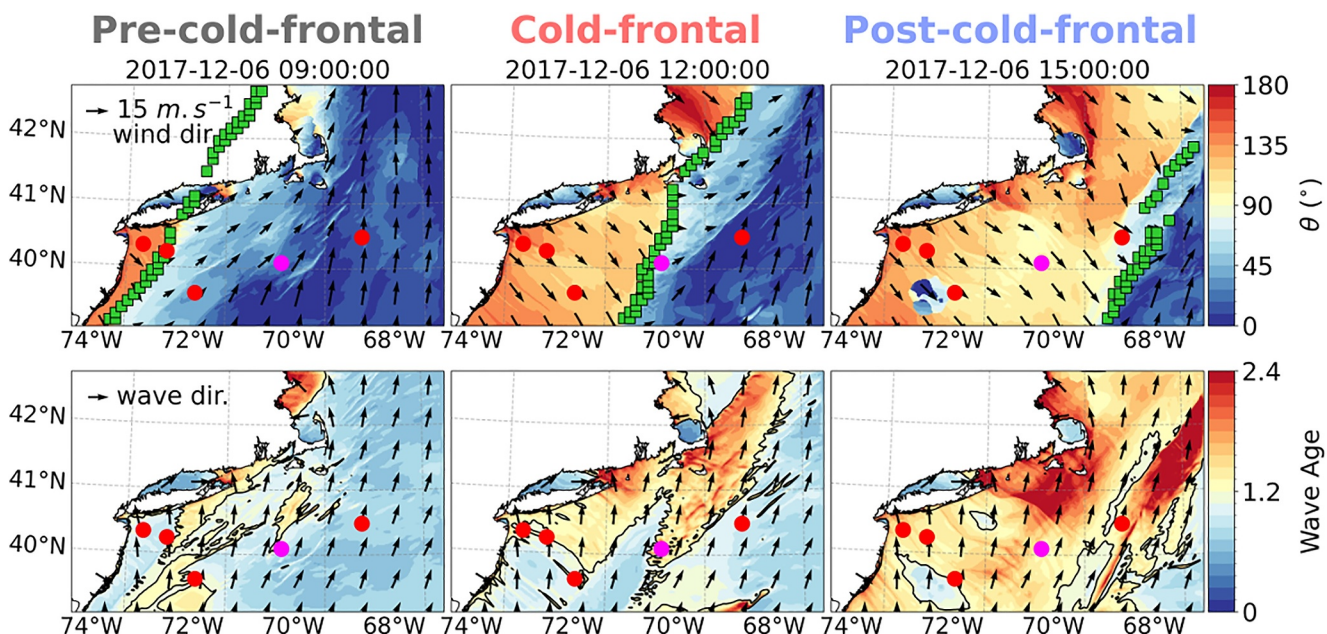


Figure 2. The top row shows the evolution of wave-wind misalignment angle, θ (shading), overlaid with the surface wind (black arrows) as simulated from the WBF θ run at (left) 09:00 (pre-cold-front), (middle) 12:00 (cold-front), and (right) 15:00 (post-cold-front) UTC on 6 December 2017. The green markers indicate the detected cold front using the Parfitt et al. (2017) algorithm. The bottom row shows the evolution of the wave age, overlaid with the wave peak direction (normalized black arrows). A wave age of 1.2 is indicated by a black contour. The magenta circles denote the location of the Pioneer Array, and the 4 red circles the NDBC moorings (from left to right: mooring identification numbers 44065, 44025, 44066, and 44008).

Two coupled model simulations are run for a 3-day case study (December 5–8, 2017) featuring one passing atmospheric front (Figure 1a). In the simulation dubbed *WBF* θ , the roughness length is parameterized by Equation 6, where the wind and wave misalignment effect is considered. This will be compared to another simulation, called *WBF*, where such an effect is omitted (Equation 5). In both simulations, the WRF model is initialized and driven by the 1-hr 0.25° ERA5 reanalysis (Hersbach et al., 2020), ROMS by the daily 1/12° MERCATOR International global reanalysis (Lellouche et al., 2018), and WW3 by 11 spectral points obtained from the global 1/2° WW3 simulations (Rascle & Arduhin, 2013). The initial conditions for WW3 were obtained from the 30-day spin-up simulations forced by ERA5 atmospheric forcing. In ROMS, the tidal forcing is obtained using the Oregon State University Tidal Prediction Software (Egbert & Erofeeva, 2002) and applied as a 2-D open boundary condition by prescribing the tidal period, elevation amplitude, current phase angle, current inclination angle, the minimum, and maximum tidal current, and ellipse semi-minor axes for 13 major tidal constituents (Steffen et al., 2023).

3. Case Study Examination

This section uses in situ observations and model simulations to examine the misaligned waves before and after the passage of an atmospheric front. To provide spatial context, we will discuss the *WBF* θ model results first. *WBF* shows similar frontal and sea state characteristics (not shown). Figure 2 compares three stages of a cold front passage, showing the directional misalignment (θ) and the wind-speed-based wave age ($\chi = c_p/U_{10}$) for three different times: December 6 at 09:00 UTC, when the Pioneer Array is ahead of the cold front (pre-cold-front), at 12:00 UTC (cold-front), and at 15:00 UTC (post-cold-front). Hereafter, U_{10} is defined as $U_{10} = (U_{10x}^2 + U_{10y}^2)^{1/2}$ where U_{10x} is the zonal and U_{10y} is the meridional wind components.

3.1. Evolutions of Winds and Waves

During the pre-cold-front, the directional misalignment is generally small ($\theta < 45^\circ$). The strong southerly and southwesterly wind (black vectors in the top row) in the warm sector is associated with the southerly waves (black vectors in the bottom row), with an overall developing sea state ($\chi < 1.2$). The wind abruptly switches to northwesterly across the cold front. In response, strongly misaligned waves with $\theta > 100^\circ$ occur over a broad fetch

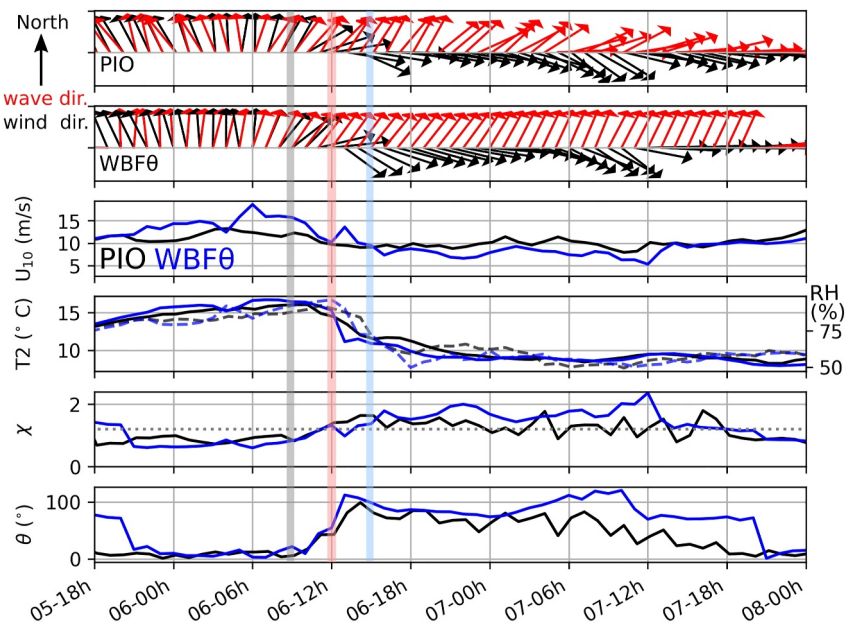


Figure 3. The top two panels show the observed and simulated ($\text{WBF}\theta$) wind direction (black arrows) and wave peak direction (red arrows) around the passing of the atmospheric front on 6 December 2017. The length of the arrows in the top two panels is normalized. Gray, red, and blue shaded periods denote the pre-cold-front, cold-front, and post-cold-front, respectively, as shown in Figure 2. The following panels show the 10-m wind speed (U_{10} , ms^{-1}), 2-m air temperature (T_2 , solid line, $^{\circ}\text{C}$), 2-m relative humidity (RH, dashed line, %), wave age, and misalignment angle (θ , $^{\circ}$) from the Pioneer Array (black) and $\text{WBF}\theta$ (blue). The dotted gray line on the wave age panel denotes the wave age = 1.2.

west of the cold front, with χ rising above 1.2. As the front moves eastward, a new area of misaligned waves is continuously generated in the far east, with the developing sea state ($\chi < 1.2$) progressively turning into a mixed sea state ($1.2 < \chi < 3$) in the far west. Much of the sea state behind the cold front is a mixture of two wave categories: slightly older southerly wind waves forced by the warm sector southerly wind and newly generated younger short wind waves forced by the cold sector northwesterly wind (Figures 2 and 3).

These wind and wave evolutions from the model are consistent with the observations at the Pioneer Array. Figure 3 shows the hourly time series of the near-surface meteorological and wave measurements. During the pre-cold-front (gray-shaded period), southerly winds (black arrows) with $>10 \text{ ms}^{-1}$ and a developing sea state ($\chi \leq 1.2$) were observed. The waves were largely aligned with the wind (red arrows). It is noted that the peak wave direction from the model generates more abrupt changes in direction compared to the observation +24 hr after the front passage. The use of the mean wave period would yield a smoother transition as the waves change direction, as seen from the observations (not shown). After the cold front passage on December 6 at 12:00 UTC (red-shaded period), the near-surface air temperature and relative humidity dropped rapidly, and the wind direction switched to northwesterly, while the dominant wave direction continued to be southerly, indicating a large degree of wave-wind misalignment ($\theta \geq 100^{\circ}$) and a mixed sea state ($\chi > 1.2$). For this particular event, the wind waves remained misaligned with the winds for more than 18 hr after the cold front, after which the waves gradually became aligned with the wind, and the wave age subsided below 1.2.

The adjacent NDBC buoys captured similar wave responses. The 2D wave spectra plots constructed from the 4 NDBC buoys (Figure 4) indicate that during the pre-cold-front, the dominant wave direction is southerly, with wave periods of 5–10 s. Even after the cold front passes, these southerly surface waves persist, while new short waves with a period lower than 5 s are generated from the northwest. While there is a reasonable range of regional variability across the buoys, the salient feature of the wave responses is broadly consistent across all the buoys examined. Compared to the Pioneer Array and the NDBC buoys, the simulation ($\text{WBF}\theta$) also captures the characteristics of the atmospheric front and the observed wave evolution reasonably well. The model also captures the background easterly swell observed from the NDBC buoys.

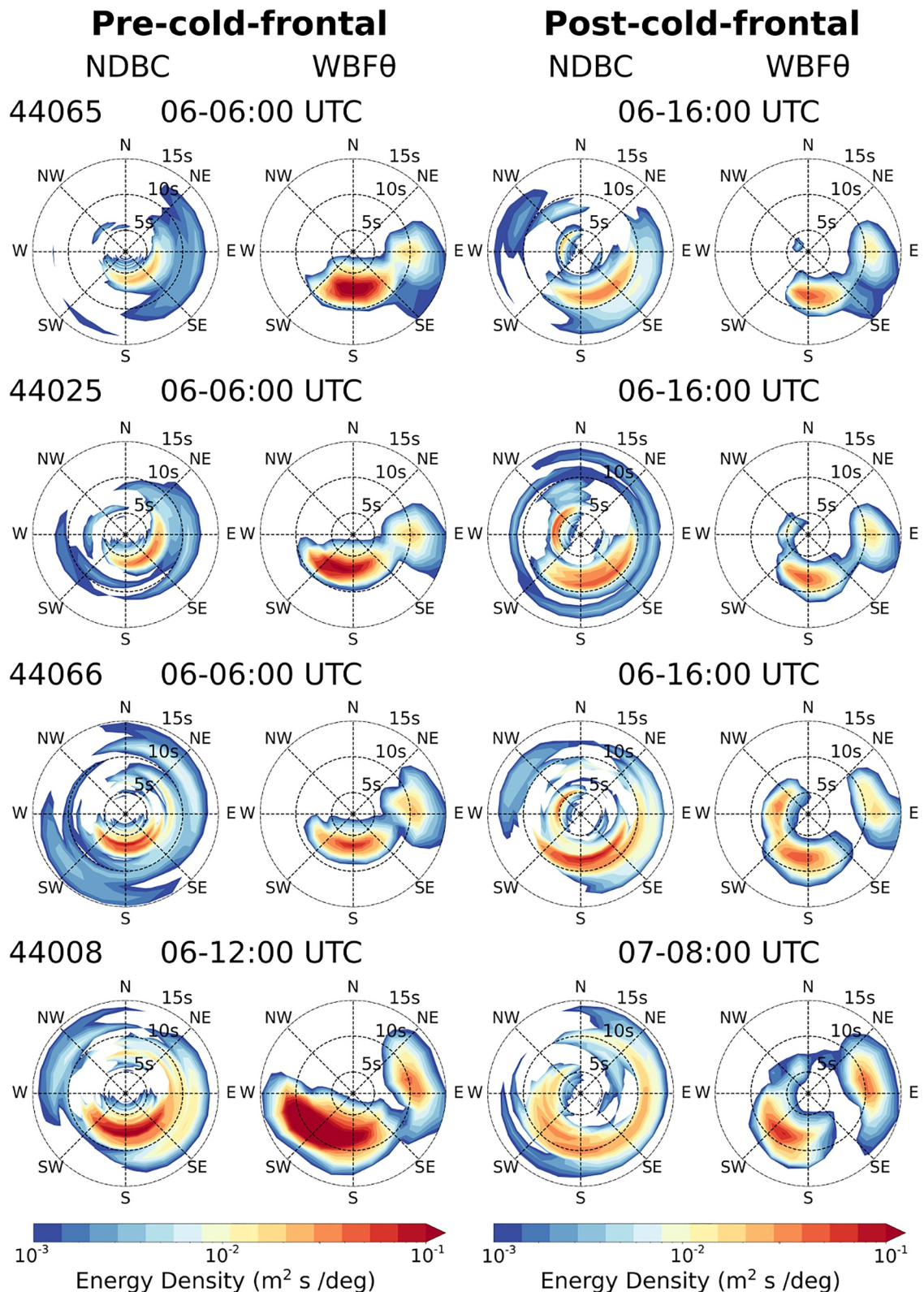


Figure 4. The 2D wave energy density spectra ($m^2 s^{-1}$) in the period space calculated from the 4 NDBC mooring locations, 44065, 44025, 44066, and 4408 (see Figure 2 for mooring locations) and the WBF θ run during the pre-cold-front (left column) and post-cold-front (right column) periods.

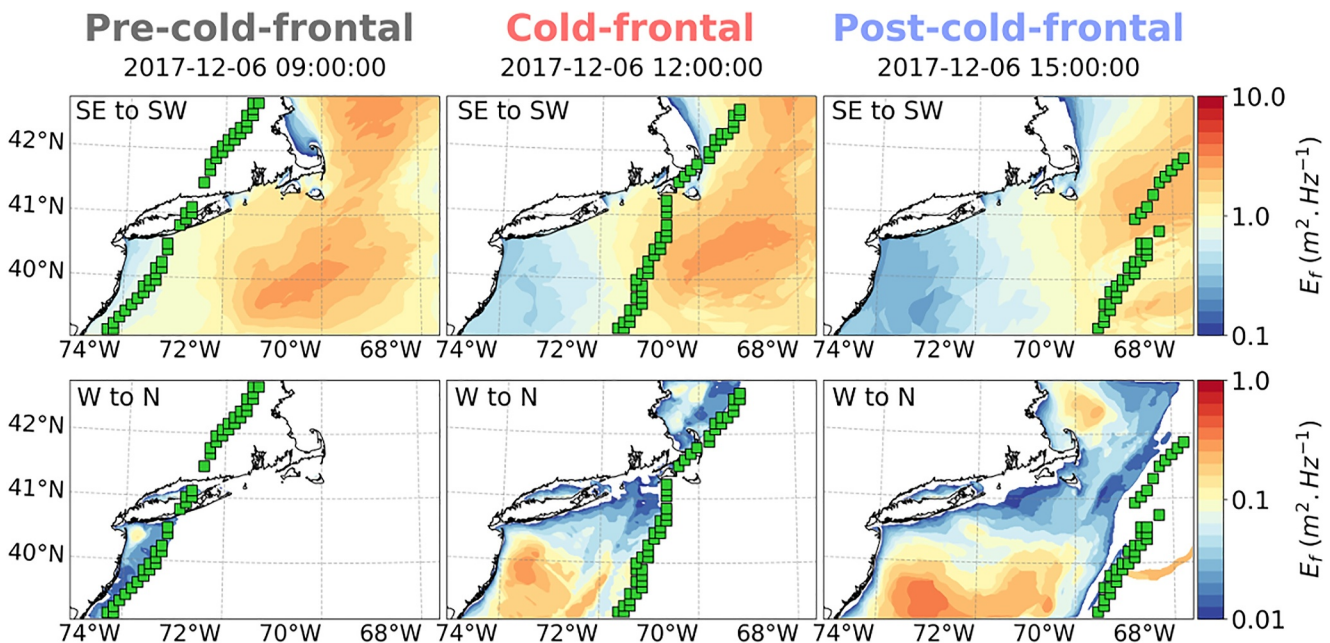


Figure 5. The frequency-averaged wave energy density spectra (E_f , m^2Hz^{-1}) from WBF θ at (left) 09:00 (pre-cold-front), (middle) 12:00 (cold-front), and (right) 15:00 (post-cold-front) UTC on 6 December 2017. The green markers indicate the detected cold front using the Parfitt et al. (2017) algorithm. The top row shows the energy coming from the 90° sectors between the southeast and southwest direction (SE to SW), while the bottom row shows the energy coming from the 90° sectors between the west and north direction (W to N).

Figure 5 shows the frequency-averaged wave energy density spectra (E_f) during the passage of the atmospheric front in WBF θ . The top row shows the average energy coming from the 90° sectors from the southwest to southeast direction, while the bottom row shows the energy coming from the 90° sectors from the west to north direction. Strong southerly wave energy builds under the warm sector ahead of the cold front and dissipates as the cold front passes over the region. Meanwhile, the northwesterly winds behind the cold front generate new waves coming from the northwest, so the wave energy from that direction grows following the cold front, creating mixed sea conditions. Note that the color scale on Figure 5 is different on both rows and indicates that the southerly energy is much stronger and dominant even after the cold front, leading to the observed wind and wave misalignment. As suggested in Figure 3, more than 18 hr after the passage of the cold front is needed for the waves to be aligned again and for the southerly wave energy under the warm sector to dissipate eventually.

3.2. Impacts on Surface Drag and Momentum Flux

The WBF θ run is compared with the WBF run to reveal the effect of misaligned waves when using Equation 6 to calculate the surface fluxes. For this, we will focus on differences in directly impacted variables: z_0 , C_D , τ , and wind speeds at two different heights, 10 m (within the surface layer, U_{10}) and 110 m (above the surface layer, U_{110}). We will also discuss the changes in turbulent heat flux after that. For simplicity, we will compare the difference only at the post-cold-front (December 6, 15:00 UTC).

The left column of Figure 6 shows WBF θ , and the right column shows the difference between WBF θ and WBF, expressed as the percentage difference ($(\text{WBF}\theta - \text{WBF})/\text{WBF} \times 100$). East of the cold front, where the wave and wind are largely aligned, little difference is found in each of these four quantities. However, sizable increases are found in z_0 , C_D , and τ west of the cold front. The increase can be as high as 300% for z_0 , 30% for C_D , and 20% for τ , respectively. If area-averaged over the broad region west of the cold front, the increases are 185.7%, 19.3%, and 11%, respectively (Figures 6a–6d). Moreover, because of the increase in the surface drag, U_{10} is reduced in WBF θ by up to 5% (or 2% when area-averaged, Figures 6g and 6h). While Equations 5 and 6 indicate that the greater the misalignment, the greater the differences, the spatial variability is very strong given the chaotic nature of the phenomenon (high winds and waves, transient weather conditions). The increased drag by the misaligned wave is also felt above the surface layer. Here, the wind at 110 m is chosen to show the impact above the surface layer (Figures 6i and 6j). U_{110} is reduced behind the cold front, having a coherent spatial pattern to that of U_{10} .

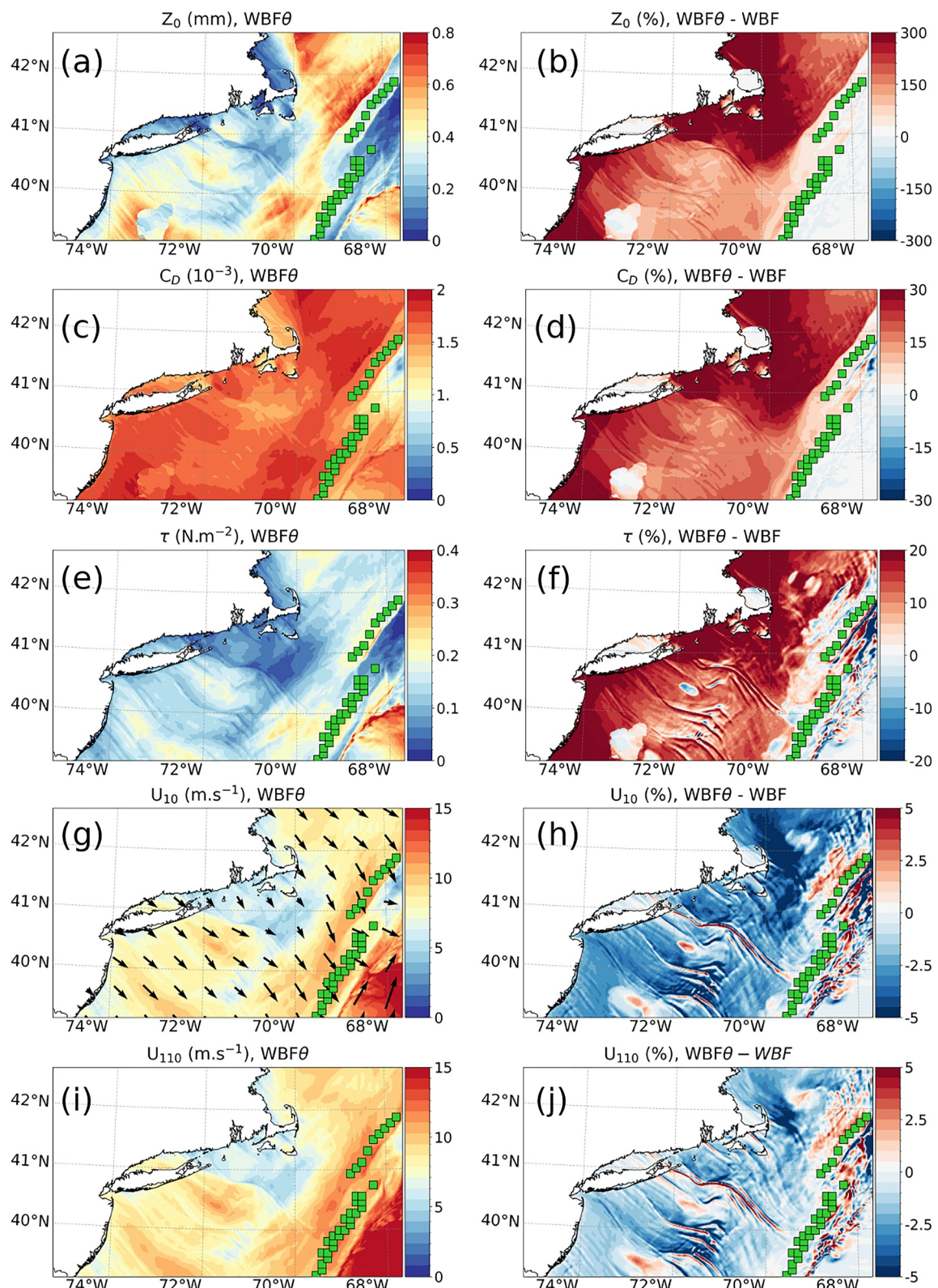


Figure 6. (a, c, e, g, i) show the roughness length (z_0), drag coefficient (C_D), momentum flux (τ), surface wind speed (U_{10}), and wind speed at 110 m (U_{110}) from WBFθ and (b, d, f, h, j) the difference between WBFθ and WBF (%) after the passage of the cold front at 15:00 UTC on 6 December 2017. The arrows overlaid on U_{10} denote the direction of the surface wind. The green markers indicate the detected cold front using the Parfitt et al. (2017) algorithm.

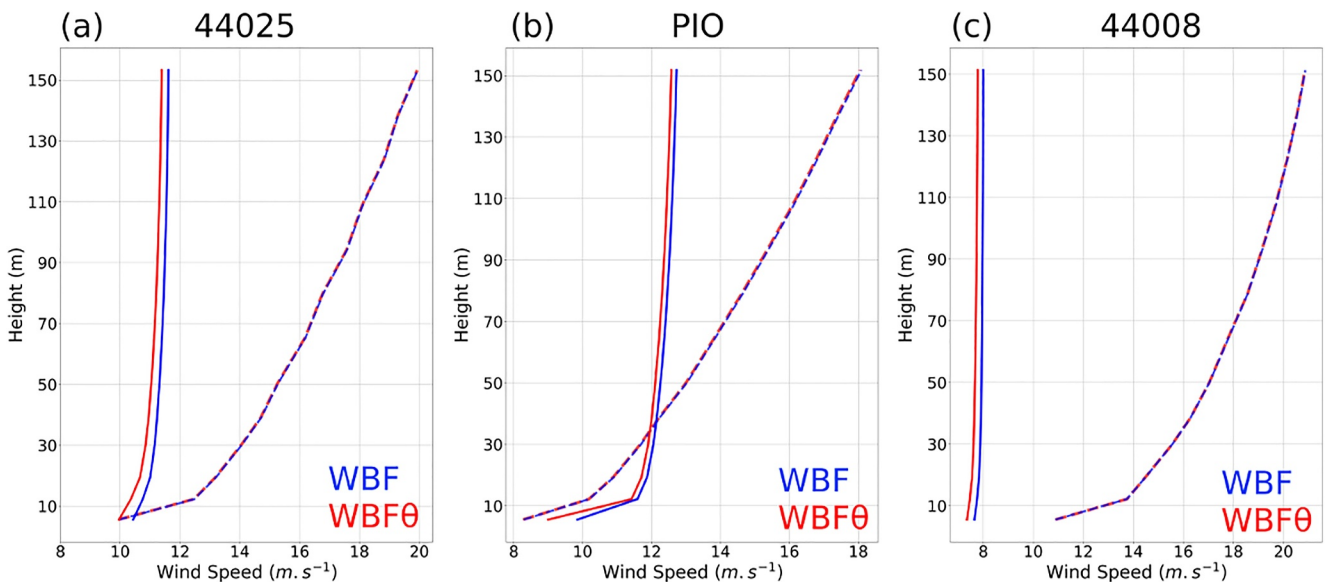


Figure 7. Vertical wind speed profiles from WBF (blue) and WBF θ (red) at (b) Pioneer Array location and (a, c) two NDBC moorings, 44025 and 44008. On each plot, a profile before (dashed) and a profile after (solid) the passage of the cold front is shown. For NDBC moorings (a, c), the times are chosen to be the same as in Figure 4, while for Pioneer Array (b), the times are chosen to be the pre-cold-front and post-cold-front shown in Figure 2.

However, the magnitude of the reduction above the surface layer is generally small (1%–5% or 0.1–0.5 m.s $^{-1}$, Figures 6i and 6j). Figure 7 shows wind speed profiles at different NDBC moorings and Pioneer Array locations, confirming that the effect of increased drag by the misaligned waves on wind speed is largest in the surface layer and smaller above it.

3.3. Impacts on Turbulent Heat Flux

The increases in surface roughness length due to misaligned waves also reduced the upward sensible heat flux (H_c) and latent heat flux (H_l) west of the cold front by up to 10% (1.5%, or $1 \sim 2 \text{ W m}^{-2}$, when area-averaged, Figures 8i, 8j, 9c, and 9d). This decrease in upward turbulent heat fluxes occurs despite a moderate increase in the exchange coefficients for heat (C_h) and moisture (C_e) by up to 5% (Figures 8c and 8d). Note that C_h and C_e are set to be identical in the COARE3.5 algorithm. To investigate in more detail the impact on heat fluxes, we recalculated using COARE3.5 offline the scalar roughness length for temperature and humidity (z_{0t} and z_{0q}), the surface exchange coefficients (C_h and C_e) and the specific humidity scaling parameter (q_s) which are not directly given by WRF outputs. The scalar roughness length for temperature, z_{0t} , is defined using the roughness Reynolds number (R_r) as:

$$R_r = \frac{u_* z_0}{\nu}, \quad (7)$$

$$z_{0t} = \frac{5.8e^{-5}}{R_r^{0.72}}, \quad (8)$$

where ν is the kinematic viscosity of the air. In COARE3.5, the moisture roughness length z_{0q} is equal to z_{0t} . The sensible and latent heat transfer coefficients are defined as

$$C_h(z, z_0, z_{0t}, \psi_m, \psi_h) = \left[\frac{\kappa}{\ln(z/z_0) - \psi_m(\zeta)} \right] \left[\frac{\kappa}{\ln(z/z_{0t}) - \psi_h(\zeta)} \right], \quad (9)$$

$$C_e(z, z_0, z_{0q}, \psi_m, \psi_h) = \left[\frac{\kappa}{\ln(z/z_0) - \psi_m(\zeta)} \right] \left[\frac{\kappa}{\ln(z/z_{0q}) - \psi_h(\zeta)} \right], \quad (10)$$

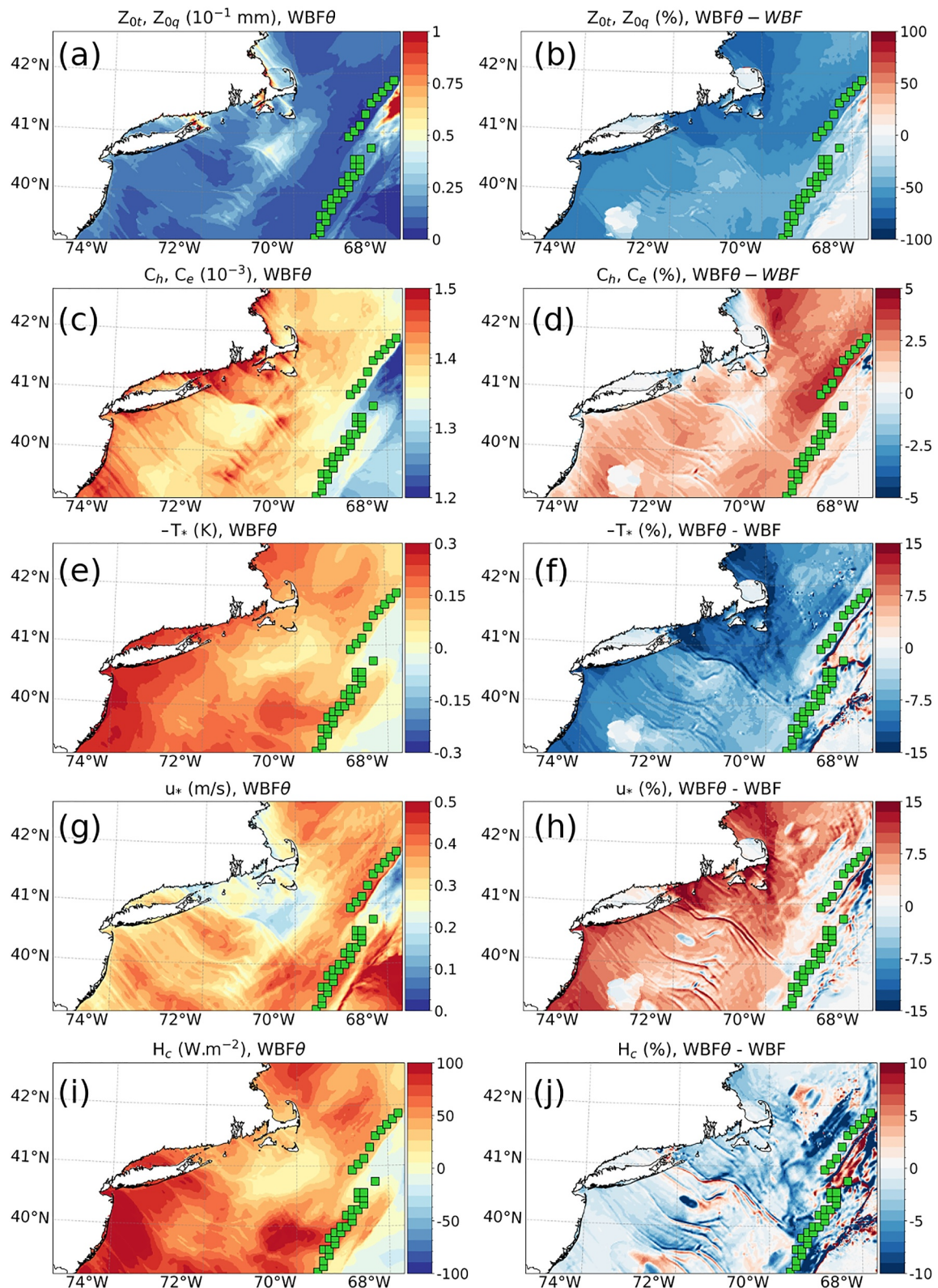


Figure 8. As in Figure 6, but for the scalar roughness length ($z_{0t}, z_{0q}, 10^{-1} \text{ mm}$), the exchange coefficient for heat and moisture ($C_h, C_e, 10^{-3}$), the temperature scaling parameter (T_*, K), the friction velocity (u^*, ms^{-1}) and the sensible heat flux (H_c, Wm^{-2}). Heat flux is defined as positive upward.

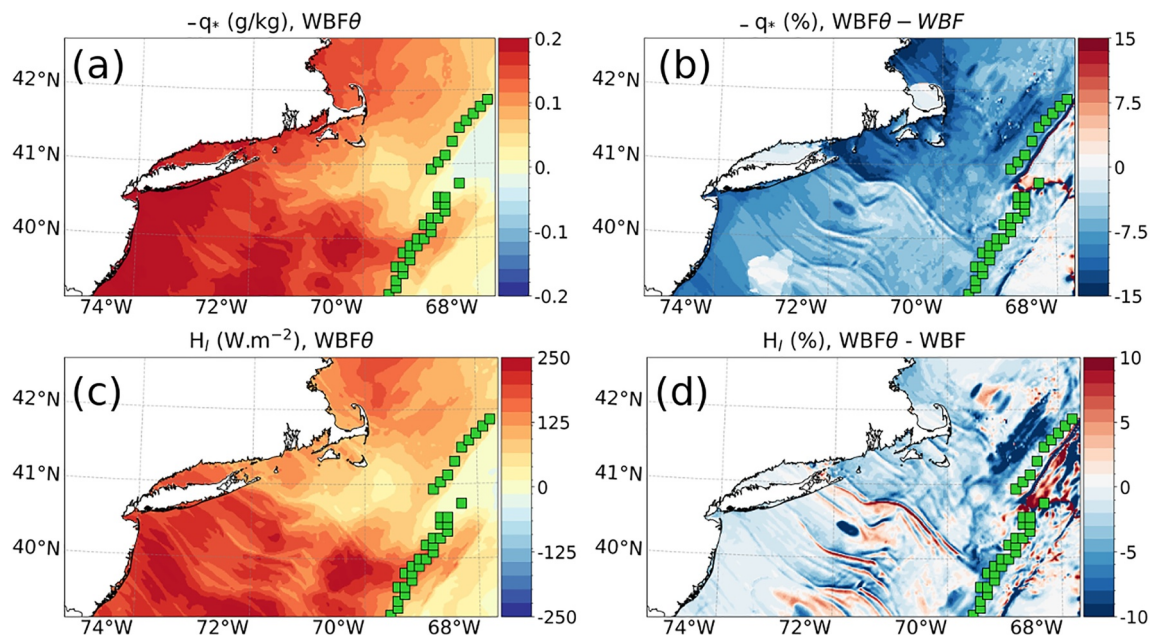


Figure 9. As in Figure 6, but for (a, b) the specific humidity scaling parameter (q_* , g/kg) and (c, d) the latent heat flux (H_l , W m $^{-2}$).

where $\psi_h(\zeta)$ is another empirical function of atmospheric stability. Because $z_{0q} = z_{0t}$ in COARE3.5, $C_e = C_h$.

The scalar roughness length z_{0t} is inversely proportional to the velocity roughness length z_0 (Equations 7 and 8). Hence, the increase in z_0 due to wave misalignment (Figures 6a and 6b) decreases z_{0t} (60% when area-averaged, Figures 8a and 8b) and the turbulent flux scale for temperature, T_* by up to 15% (5% when area-averaged) behind the cold front (Figures 8e and 8f). Note that T_* and the turbulent moisture flux scale q_* are defined to be negative for heat fluxes out of the ocean, so we plot $-T_*$ and $-q_*$ so that positive values of these quantities correspond to positive values of H_c and H_l . Overall, the increase in u^* (4% on average) due to misalignment (Figures 8g and 8h, Equation 2) is more than offset by the decrease in $-T_*$, resulting in a 1.5% decrease on average in H_c . Similarly, the decrease in z_{0q} decreases in $-q_*$, which compensates for the increase in u^* , resulting in a 1.5% decrease on average in H_l (Equation 3, Figure 9).

4. Long-Term Characterization

Multi-year measurements of near-surface meteorology, surface waves, and direct covariance fluxes from the Pioneer Array are used to examine the long-term characteristics of the misaligned waves under cold fronts. To do that, we first have to detect the cold front from the buoys. Because the Pioneer Array data are surface-based observations, the detected fronts in this section should be deemed surface cold fronts. Based on the meridional surface wind (U_{10y}) and the 2-m air temperature (T2), at each hour, the cold front is identified when U_{10y} is shifted from southerly to northerly, with an additional criterion that the northerly (southerly) U_{10y} must persist over 2 hr after (before) the frontal passage. We then check for a decrease in T2 by $>3^\circ\text{C}$ between $t = -2$ hr and $t = +8$ hr. To capture the cold front events with a strong shift in wind direction at the passage of the cold front, an additional criterion is applied such that a change in wind direction should be at least 60° . If all these conditions are met, the event is considered an atmospheric cold front over the Pioneer Array at $t = 0$. Based on this set of criteria, 86 atmospheric cold fronts were identified from the entire 8-year Pioneer Array data set. Fifty-five of these events have co-located measurements of surface waves, which are used for subsequent analysis. Hereafter, we defined misaligned waves when the angle between wind and wave directions exceeds 60° . The number of atmospheric cold fronts and the misaligned waves vary with the chosen empirical thresholds. However, the results do not change appreciably with reasonable variations of these thresholds.

Figure 10a shows the histogram of the so-detected cold front occurrence as a function of calendar months. Consistent with the previous studies (Parfitt et al., 2017; Reeder et al., 2021), the cold fronts are most frequently

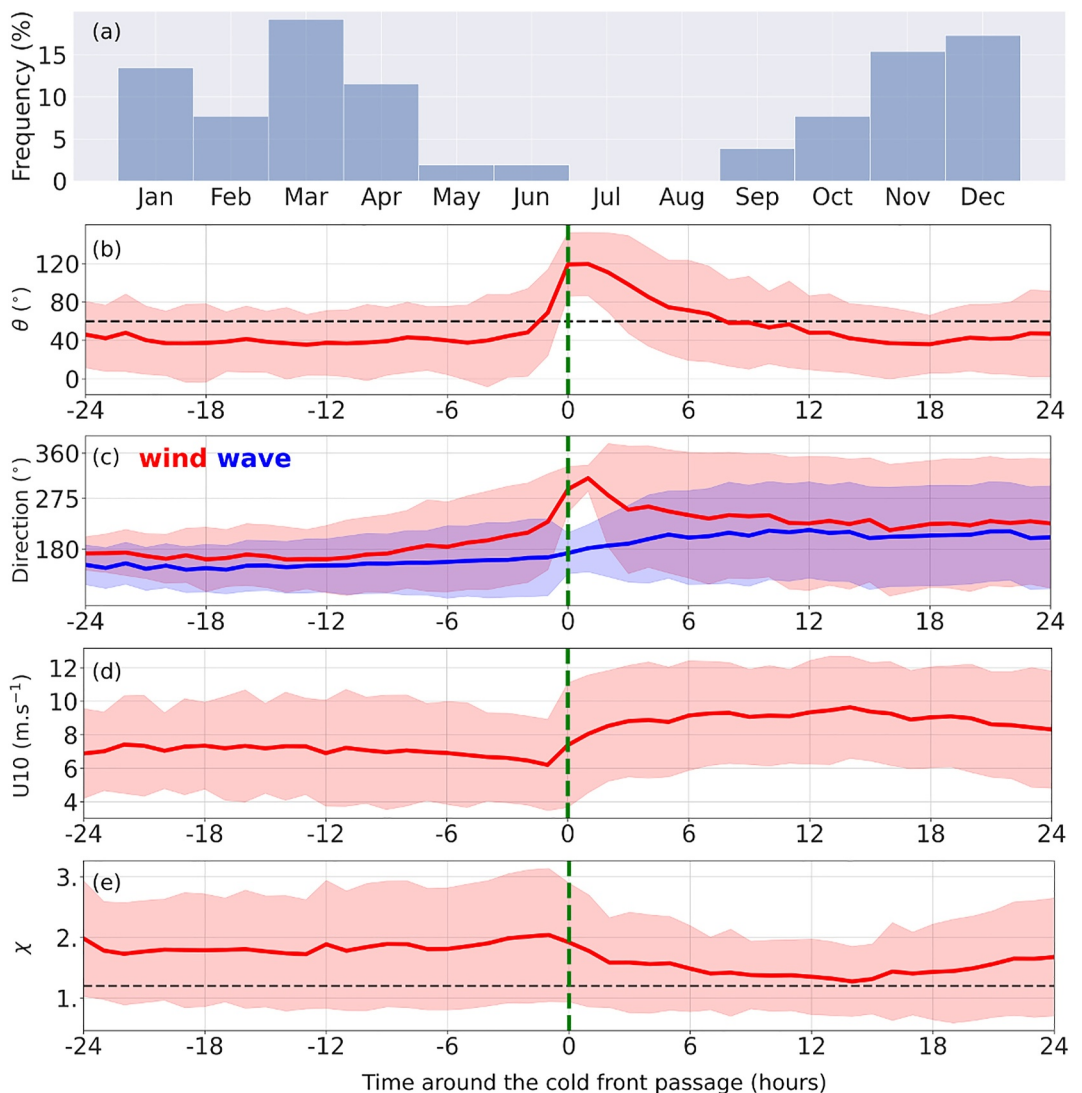


Figure 10. (a) The probability of occurrence of a cold front per month (%) calculated using the Pioneer Array data from December 2014 to November 2022. (b, c, d, e) Composite evolutions of (b) misalignment angle (θ , $^{\circ}$), (c) wind and wave direction ($^{\circ}$, 0 means northerly), (d) wind speed ($m s^{-1}$), and (e) wave age for the detected atmospheric cold fronts. The shaded envelopes represent ± 1 standard deviations. The dashed line indicates the 60° misalignment threshold in panel (b) and a wave age of 1.2 in panel (e). The vertical green line indicates the cold front at $t = 0$.

observed during the extended winter period (November–March), with 62 out of 86 events. Figure 10b shows the composite evolutions of θ across the fronts, indicating strongly misaligned waves at the cold front passage ($t = 0$).

These fronts feature southerly wind (Figure 10c) with moderate speed ($8 m s^{-1}$, Figure 10d) in the warm sector accompanied by a strong shift in wind direction from the warm to cold sectors exceeding at least 60° (Figure 10c). Because of moderate wind conditions in the warm sector, the sea state is characterized by a mixed sea ($1.2 < \chi < 2$), where wind-waves and background swell co-exist, the condition that was also observed from the NDBC buoys (Figure 4). As the cold front passes and the winds change the direction, the waves begin to be misaligned $1 \sim 2$ hr before the front, and once generated, the waves remain misaligned for 8 hr on average (Figure 10b).

We use the DCFS momentum flux measurements at the Pioneer Array to evaluate the accuracy of the parameterized momentum flux. Because DCFS data are available for a shorter period (see Section 2.1), only 36 atmospheric front events were identified from this period, of which 20 have led to strongly misaligned waves ($\theta > 60^{\circ}$). Some cold front events did not lead to strongly misaligned waves because they were accompanied by

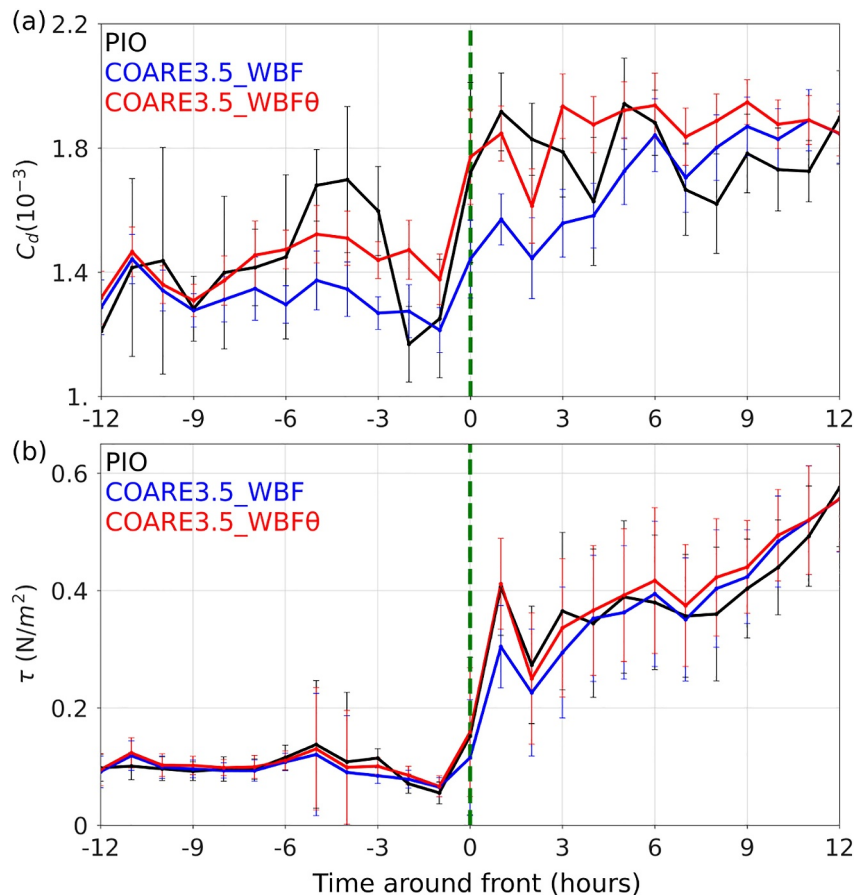


Figure 11. Composite evolution of the median of the parameterized (a) drag coefficient (C_d , 10^{-3}) and (b) momentum flux (τ , Nm^{-2}) calculated offline using the COARE3.5 (COARE3.5_WBF θ , red) with and (COARE3.5_WBF, blue) without the misaligned wave effect, in comparison to direct covariance flux measurements from the Pioneer Array (PIO, black). The error bars represent ± 1 standard error. The vertical green line indicates the cold front at $t = 0$.

the westerly winds, not the northwesterly winds (not shown). Note that surface waves are from the south; hence, the westerly winds over the southerly waves do not cross the criterion of $\theta > 60^\circ$ to be defined as misaligned waves. The different choices of threshold angle would yield different numbers of cold fronts leading to misaligned waves; however, reasonable variations of the threshold value (45–70°) do not change the results significantly.

Figures 11a and 11b shows the composite evolutions of the median of the directly measured C_d and τ (black) from the Pioneer Array for the fronts that generated the misaligned waves. With the state variables measured from the Pioneer Array, we then calculated C_d and τ using the COARE algorithm without considering the misaligned waves effect (COARE3.5_WBF in blue, Equation 5) and considering the misaligned waves effect (COARE3.5_WBF θ in red, Equation 6). The result shows that the estimated momentum flux with misaligned waves effect is higher than that without by 16.5% at $t = 0$ and 5.2% for 8 hr after the cold front. When averaged over the 8 hr after the cold front, this elevated wind stress with misaligned waves effect is closer to the DCFS estimates (the mean bias is reduced from 6.5% to 5.2% for τ and from 7.6% to 3.5% for C_d). The results also corroborate the modeling results (WBF vs. WBF θ). However, during the pre-front and post-front (+6 hr to +12 hr), COARE3.5_WBF and COARE3.5_WBF θ underestimate and overestimate the drag coefficient, respectively. This suggests further tuning of the parameterizations is needed to improve the accuracy of the formulation by better representing the misaligned wave impacts in COARE.

5. Conclusion and Discussions

Using the multi-year in-situ observations and high-resolution ocean-atmosphere-wave fully coupled model simulations, this study examined the nature and impacts of the misaligned surface waves behind the passing of

atmospheric cold fronts off the coast of New England. A case study investigation indicates that an atmospheric cold front generates a significant fetch of misaligned waves, comparable to the lateral extent of the extratropical cyclone in which the front is embedded. Over a vast region of misaligned waves propagating with the front, the coupled model simulation indicates that misaligned waves significantly increase the roughness length, drag and enthalpy exchange coefficients, and wind stress. In response to increased surface drag (20%), the near-surface wind speed is reduced (2%), reducing upward turbulent heat fluxes (1.5%), indicative of a weak feedback effect on the atmosphere. The decrease in upward turbulent heat flux is despite the moderate increase in surface heat and moisture exchange coefficients. The friction velocity increases on average by 4% due to the misaligned waves. However, because the scalar roughness decreases as the velocity roughness increases, the misaligned waves also reduce the temperature and humidity scaling parameters on average by 5%. The net effect of this offset is a modest decrease in the upward sensible and latent heat flux.

We also examined the directly measured versus parameterized momentum fluxes from the Pioneer Array under all atmospheric cold fronts that generated misaligned waves. The modified COARE algorithm that takes into account the misaligned wave effect (Equation 6) produced enhanced momentum flux by 16.5% compared to the default formulation without the misaligned wave effect (Equation 5). We show that the former estimate is more consistent with the directly measured stress.

The current COARE wave-based bulk flux parameterization assumes that waves and wind are aligned (Equation 5). A simple modification to this formulation is suggested to represent the surface roughness length increase due to the misaligned wave effect as in Equation 6, which produces overall improved estimates of the parameterized momentum flux under this condition. As discussed extensively in Sauvage et al. (2023), equivalent to incorporating the directional misalignment in COARE is replacing the peak wave period with the mean wave period to calculate the wave age in Equation 5 (See their Eq. 12). The rationale is that the spectrally averaged wave period more accurately depicts a sea state that is a mixture of wind waves of ranging frequencies, as in Figure 4.

By explicitly accounting for the wind-wave misalignment in the commonly used advanced air-sea flux parameterizations under mid-latitude storms, this study contributes to the growing body of literature on the directional wave-wind coupling effects on surface drag and air-sea fluxes. Previous studies using available observations and Large Eddy Simulation in shallow oceans or under tropical cyclone-induced high winds have found the drag coefficient to decrease as the misalignment increases (e.g., S. Chen et al., 2022; Manzella et al., 2024; Potter et al., 2022; Zhou et al., 2022). These studies also found varied drag coefficient responses depending on the degree of alignment between the wind and the waves, that is, whether the waves are following, opposing, or coming in oblique to the wind (i.e., Holthuijsen et al., 2012; Husain et al., 2022a, 2022b). In addition, recent studies have found that, under swell-dominated conditions, the surface drag coefficient increases as the misalignment increases (Li, 2023; Patton et al., 2019; Porchetta et al., 2019, 2021; Sauvage et al., 2023). These varied responses in the surface drag to the misaligned short-wind and swell waves demonstrate a strong regime dependence of the phenomenon, pointing to the need for systematic observational and modeling investigation of a wide range of wind and wave regimes to inform and improve the air-sea flux parameterization.

Finally, the impacts of the improved surface stress on the wind profile appear limited to the surface layer. An important caveat is that this specific conclusion mainly concerns the “instantaneous” impacts of the altered momentum flux on the atmosphere, whereas, in the nature and long-term coupled runs, the mixed layer depth will likely respond to different turbulent momentum and heat fluxes, thereby greatly affecting state variables such as sea surface temperature. We anticipate that such an indirect process involving the near-surface turbulent mixing, stratification, and sea surface temperature will likely be an important factor for the atmospheric feedback effect. However, this effect cannot be captured in the short 3-day simulations conducted in this study. Longer simulations are needed to determine the impacts on kinematic and thermodynamic properties in the PBL and upper ocean and possibly their effect on the evolution of the atmospheric fronts.

Data Availability Statement

ERA5 data are made available by Copernicus Climate Change Service (<https://doi.org/10.24381/cds.adbb2d47>), Mercator by Copernicus Marine Environment Monitoring Service (<https://doi.org/10.48670/moi-00016>), and global 3-hourly spectral wave analyses by Ifremer is available via an FTP server (<ftp://ftp.ifremer.fr/ifremer/>

ww3/HINDCAST/GLOBAL). OOI Pioneer Array data are obtained from <https://erddap.dataexplorer.ocean-observatories.org>, and NDBC data from <https://www.ndbc.noaa.gov/>. WW3 is distributed via <https://github.com/NOAA-EMC/WW3>, WRF <https://github.com/wrf-model/WRF>, and ROMS <https://www.myroms.org/>. The SCOAR codes are available via <https://github.com/SCOAR-model/SCOAR>. The modified COARE3.5 code is available at https://github.com/cesarsauvage/COARE3.5_modified_Sauvage-et-al._2023 and the model outputs on ZENODO at <https://zenodo.org/records/11624020>.

Acknowledgments

This research was supported by NASA (80NSSC21K1524), NSF (OCE-2148120, OCE-2022846), NOAA (NA19OAR4310376, NA22OAR4310598), and DOE (DE-EE00009424). This material is based upon work supported by the Ocean Observatories Initiative (OOI), a major facility fully funded by the National Science Foundation under Cooperative Agreement No. 2244833, and the Woods Hole Oceanographic Institution OOI Program Office. The WHOI High-Performance Computing Facility provided the computing resources. The authors thank anonymous reviewers for their comments that helped to improve the manuscript.

References

- Ardhuin, F., O'Reilly, W. C., Herbers, T. H. C., & Jessen, P. F. (2003). Swell transformation across the continental shelf. Part I: Attenuation and directional broadening. *Journal of Physical Oceanography*, 33(9), 1921–1939. [https://doi.org/10.1175/1520-0485\(2003\)033\(1921:STATCS\)2.0.CO;2](https://doi.org/10.1175/1520-0485(2003)033(1921:STATCS)2.0.CO;2)
- Ardhuin, F., & Roland, A. (2012). Coastal wave reflection, directional spread, and seismoacoustic noise sources. *Journal of Geophysical Research*, 117(C11). <https://doi.org/10.1029/2011JC007832>
- Babanin, A. (2011). *Breaking and dissipation of ocean surface waves*. Cambridge University Press. <https://doi.org/10.1017/CBO9780511736162>
- Battjes, J. A., & Janssen, J. P. F. M. (1978). Energy loss and set-up due to breaking of random waves. *Coastal Engineering*, 569–587. <https://doi.org/10.1061/9780872619094.034>
- Berry, G., Reeder, M. J., & Jakob, C. (2011). A global climatology of atmospheric fronts. *Geophysical Research Letters*, 38(4). <https://doi.org/10.1029/2010GL046451>
- Bjerknes, J., & Solberg, H. (1922). Life of the cyclones and the polar front theory of atmospheric circulation. *Geophysiks Publikationer*, 3(1), 18.
- Cao, Y., Li, C., & Dong, C. (2020). Atmospheric cold front-generated waves in the coastal Louisiana. *Journal of Marine Science and Engineering*, 8(11), 900. <https://doi.org/10.3390/jmse8110900>
- Catto, J. L., & Pfahl, S. (2013). The importance of fronts for extreme precipitation. *Journal of Geophysical Research: Atmospheres*, 118(19), 10791–10801. <https://doi.org/10.1002/jgrd.50852>
- Chen, F., & Dudhia, J. (2001). Coupling an advanced land surface–Hydrology model with the Penn State–NCAR MM5 modeling system. Part I: Model implementation and sensitivity. *Monthly Weather Review*, 129(4), 569–585. [https://doi.org/10.1175/1520-0493\(2001\)129\(0569:CAALSH\)2.0.CO;2](https://doi.org/10.1175/1520-0493(2001)129(0569:CAALSH)2.0.CO;2)
- Chen, G., Chapon, B., Ezraty, R., & Vandemark, D. (2002). A global view of swell and wind sea climate in the Ocean by satellite altimeter and scatterometer. *Journal of Atmospheric and Oceanic Technology*, 19(11), 1849–1859. [https://doi.org/10.1175/1520-0426\(2002\)019\(1849:AGVOSA\)2.0.CO;2](https://doi.org/10.1175/1520-0426(2002)019(1849:AGVOSA)2.0.CO;2)
- Chen, S., Qiao, F., Zhang, J. A., Xue, Y., Ma, H., & Chen, S. (2022). Observed drag coefficient asymmetry in a tropical cyclone. *Journal of Geophysical Research: Oceans*, 127(9), e2021JC018360. <https://doi.org/10.1029/2021JC018360>
- Chen, S. S., & Curcic, M. (2016). Ocean surface waves in Hurricane Ike (2008) and Superstorm Sandy (2012): Coupled model predictions and observations. *Ocean Modelling*, 103, 161–176. <https://doi.org/10.1016/j.ocemod.2015.08.005>
- Chen, S. S., Zhao, W., Donelan, M. A., & Tolman, H. L. (2013). Directional wind–wave coupling in fully coupled atmosphere–wave–ocean models: Results from CBLAST-Hurricane. *Journal of the Atmospheric Sciences*, 70(10), 3198–3215. <https://doi.org/10.1175/JAS-D-12-0157.1>
- Chen, X., Ginis, I., & Hara, T. (2020). Impact of shoaling ocean surface waves on wind stress and drag coefficient in coastal waters: 2. Tropical cyclones. *Journal of Geophysical Research: Oceans*, 125(7), e2020JC016223. <https://doi.org/10.1029/2020JC016223>
- Edson, J. B., Jampana, V., Weller, R. A., Bigorre, S. P., Plueddemann, A. J., Fairall, C. W., et al. (2013). On the exchange of momentum over the open ocean. *Journal of Physical Oceanography*, 43(8), 1589–1610. <https://doi.org/10.1175/JPO-D-12-0173.1>
- Egbert, G. D., & Erofeeva, S. Y. (2002). Efficient inverse modeling of barotropic ocean tides. *Journal of Atmospheric and Oceanic Technology*, 19(2), 183–204. [https://doi.org/10.1175/1520-0426\(2002\)019\(0183:EIMOB\)2.0.CO;2](https://doi.org/10.1175/1520-0426(2002)019(0183:EIMOB)2.0.CO;2)
- Fairall, C. W., Bradley, E. F., Hare, J. E., Grachev, A. A., & Edson, J. B. (2003). Bulk parameterization of air-sea fluxes: Updates and verification for the COARE algorithm. *Journal of Climate*, 16(4), 571–591. [https://doi.org/10.1175/1520-0442\(2003\)016\(0571:BPOASF\)2.0.CO;2](https://doi.org/10.1175/1520-0442(2003)016(0571:BPOASF)2.0.CO;2)
- Fairall, C. W., Bradley, E. F., Rogers, D. P., Edson, J. B., & Young, G. S. (1996). Bulk parameterization of air-sea fluxes for tropical ocean-global atmosphere coupled-ocean atmosphere response experiment. *Journal of Geophysical Research*, 101(C2), 3747–3764. <https://doi.org/10.1029/95JC03205>
- Grachev, A. A., & Fairall, C. W. (2001). Upward momentum transfer in the marine boundary layer. *Journal of Physical Oceanography*, 31(7), 1698–1711. [https://doi.org/10.1175/1520-0485\(2001\)031\(1698:UMTITM\)2.0.CO;2](https://doi.org/10.1175/1520-0485(2001)031(1698:UMTITM)2.0.CO;2)
- Guo, B., Subrahmanyam, M. V., & Li, C. (2020). Waves on Louisiana continental shelf influenced by atmospheric fronts. *Scientific Reports*, 10(1), 272. <https://doi.org/10.1038/s41598-019-55578-w>
- Haidvogel, D. B., Arango, H. G., Hedstrom, K., Beckmann, A., Malanotte-Rizzoli, P., & Schepetkin, A. F. (2000). Model evaluation experiments in the North Atlantic Basin: Simulations in nonlinear terrain-following coordinates. *Dynamics of Atmospheres and Oceans*, 32(3), 239–281. [https://doi.org/10.1016/S0377-0265\(00\)00049-X](https://doi.org/10.1016/S0377-0265(00)00049-X)
- Hanley, K. E., & Belcher, S. E. (2008). Wave-driven wind jets in the marine atmospheric boundary layer. *Journal of the Atmospheric Sciences*, 65(8), 2646–2660. <https://doi.org/10.1175/2007JAS2562.1>
- Hanley, K. E., Belcher, S. E., & Sullivan, P. P. (2010). A global climatology of wind–wave interaction. *Journal of Physical Oceanography*, 40(6), 1263–1282. <https://doi.org/10.1175/2010JPO4377.1>
- Hasselmann, S., Hasselmann, K., Allender, J. H., & Barnett, T. P. (1985). Computations and parameterizations of the nonlinear energy transfer in a gravity-wave spectrum. Part II: Parameterizations of the nonlinear energy transfer for application in wave models. *Journal of Physical Oceanography*, 15(11), 1378–1391. [https://doi.org/10.1175/1520-0485\(1985\)015\(1378:CAPOTN\)2.0.CO;2](https://doi.org/10.1175/1520-0485(1985)015(1378:CAPOTN)2.0.CO;2)
- Hersbach, H., Bell, B., Berrisford, P., Hirahara, S., Horányi, A., Muñoz-Sabater, J., et al. (2020). The ERA5 global reanalysis. *Quarterly Journal of the Royal Meteorological Society*, 146(730), 1999–2049. <https://doi.org/10.1002/qj.3803>
- Hewson, T. D. (1998). Objective fronts. *Meteorological Applications*, 5(1), 37–65. <https://doi.org/10.1017/S1350482798000553>
- Holthuijsen, L. H., Powell, M. D., & Pietrzak, J. D. (2012). Wind and waves in extreme hurricanes. *Journal of Geophysical Research*, 117(C9). <https://doi.org/10.1029/2012JC007983>
- Hong, S.-Y., & Lim, J.-O. J. (2006). The WRF single-moment 6-class microphysics scheme (WSM6). *JOURNAL OF THE KOREAN METEOROLOGICAL SOCIETY*.

- Hsu, J.-Y., Lien, R.-C., D'Asaro, E. A., & Sanford, T. B. (2019). Scaling of drag coefficients under five tropical cyclones. *Geophysical Research Letters*, 46(6), 3349–3358. <https://doi.org/10.1029/2018GL081574>
- Husain, N. T., Hara, T., & Sullivan, P. P. (2022a). Wind turbulence over misaligned surface waves and air–sea momentum flux. Part II: Waves in oblique wind. *Journal of Physical Oceanography*, 52(1), 141–159. <https://doi.org/10.1175/JPO-D-21-0044.1>
- Husain, N. T., Hara, T., & Sullivan, P. P. (2022b). Wind turbulence over misaligned surface waves and air–sea momentum flux. Part I: Waves following and opposing wind. *Journal of Physical Oceanography*, 52(1), 119–139. <https://doi.org/10.1175/JPO-D-21-0043.1>
- Iacono, M. J., Delamere, J. S., Mlawer, E. J., Shephard, M. W., Clough, S. A., & Collins, W. D. (2008). Radiative forcing by long-lived greenhouse gases: Calculations with the AER radiative transfer models. *Journal of Geophysical Research*, 113(D13). <https://doi.org/10.1029/2008JD009944>
- Jiménez, P. A., Dudhia, J., González-Rouco, J. F., Navarro, J., Montávez, J. P., & García-Bustamante, E. (2012). A revised scheme for the WRF surface layer formulation. *Monthly Weather Review*, 140(3), 898–918. <https://doi.org/10.1175/MWR-D-11-00056.1>
- Kim, J.-Y., Kaihatu, J., Chang, K.-A., Sun, S.-H., Huff, T. P., & Feagin, R. A. (2020). Effect of cold front-induced waves along wetlands boundaries. *Journal of Geophysical Research: Oceans*, 125(12), e2020JC016603. <https://doi.org/10.1029/2020JC016603>
- Kukulka, T., & Hara, T. (2005). Momentum flux budget analysis of wind-driven air-water interfaces. *Journal of Geophysical Research*, 110(C12). <https://doi.org/10.1029/2004JC002844>
- Lellouche, J.-M., Greiner, E., Le Galloudec, O., Garric, G., Regnier, C., Drevillon, M., et al. (2018). Recent updates to the Copernicus Marine Service global ocean monitoring and forecasting real-time 1/12° high-resolution system. *Ocean Science*, 14(5), 1093–1126. <https://doi.org/10.5194/os-14-1093-2018>
- Li, S. (2023). On the consistent parametric description of the wave age dependence of the sea surface roughness. *Journal of Physical Oceanography*, 53(9), 2281–2290. <https://doi.org/10.1175/JPO-D-23-0021.1>
- Liu, Q., Rogers, W. E., Babanin, A. V., Young, I. R., Romero, L., Zieger, S., et al. (2019). Observation-based source terms in the third-generation wave model WAVEWATCH III: Updates and verification. *Journal of Physical Oceanography*, 49(2), 489–517. <https://doi.org/10.1175/JPO-D-18-0137.1>
- Makin, V. K., Kudryavtsev, V. N., & Mastenbroek, C. (1995). Drag of the sea surface. *Boundary-Layer Meteorology*, 73(1), 159–182. <https://doi.org/10.1007/BF00708935>
- Manzella, E., Hara, T., & Sullivan, P. P. (2024). Reduction of drag coefficient due to misaligned wind-waves. *Journal of Geophysical Research: Oceans*, 129(5), e2023JC020593. <https://doi.org/10.1029/2023JC020593>
- Nakanishi, M., & Niino, H. (2009). Development of an improved turbulence closure model for the atmospheric boundary layer. *Journal of the Meteorological Society of Japan. Ser. II*, 87(5), 895–912. <https://doi.org/10.2151/jmsj.87.895>
- NSF Ocean Observatories Initiative. (2023). Direct covariance flux data (Reference Designator CP01CNSM-SBD12-08-FDCHPA000), the mean meteorological data (Reference Designators CP01CNSM-SBD11-06-METBKA000 and CP01CNSM-SBD12-06-METBKA000) and wave data (Reference Designator CP01CNSM-SBD12-05-WAVSSA000) are from the Pioneer NES Array from 2015-05-13 to 2019-04-07. Direct covariance flux data are generated from the raw data archive at <https://oceanoobservatories.org/data-access/raw-data-archive/> while other dataset are available on the Data Explorer ERDDAP at <https://erddap.dataexplorer.oceanoobservatories.org>
- Parfitt, R., Czaja, A., Minobe, S., & Kuwano-Yoshida, A. (2016). The atmospheric frontal response to SST perturbations in the Gulf Stream region. *Geophysical Research Letters*, 43(5), 2299–2306. <https://doi.org/10.1002/2016GL067723>
- Parfitt, R., Czaja, A., & Seo, H. (2017). A simple diagnostic for the detection of atmospheric fronts. *Geophysical Research Letters*, 44(9), 4351–4358. <https://doi.org/10.1002/2017GL073662>
- Patton, E. G., Sullivan, P. P., Kosović, B., Dudhia, J., Mahrt, L., Žagar, M., & Marić, T. (2019). On the influence of swell propagation angle on surface drag. *Journal of Applied Meteorology and Climatology*, 58(5), 1039–1059. <https://doi.org/10.1175/JAMC-D-18-0211.1>
- Phillips, O. M. (1966). The dynamics of the upper ocean.
- Porchetta, S., Temel, O., Muñoz-Esparza, D., Reuder, J., Monbaliu, J., Van Beeck, J., & Van Lipzig, N. (2019). A new roughness length parameterization accounting for wind–wave (mis)alignment. *Atmospheric Chemistry and Physics*, 19(10), 6681–6700. <https://doi.org/10.5194/acp-19-6681-2019>
- Porchetta, S., Temel, O., Warner, J., Muñoz-Esparza, D., Monbaliu, J., Van Beeck, J., & Van Lipzig, N. (2021). Evaluation of a roughness length parameterization accounting for wind–wave alignment in a coupled atmosphere–wave model. *Quarterly Journal of the Royal Meteorological Society*, 147(735), 825–846. <https://doi.org/10.1002/qj.3948>
- Potter, H., Collins, C. O., & Ortiz-Suslow, D. G. (2022). Pier-based measurements of Air-Sea momentum fluxes over shoaling waves during DUNEX. *Journal of Geophysical Research: Oceans*, 127(11), e2022JC018801. <https://doi.org/10.1029/2022JC018801>
- Rascle, N., & Ardhuin, F. (2013). A global wave parameter database for geophysical applications. Part 2: Model validation with improved source term parameterization. *Ocean Modelling*, 70, 174–188. <https://doi.org/10.1016/j.ocemod.2012.12.001>
- Reeder, M. J., Spengler, T., & Spensberger, C. (2021). The effect of sea surface temperature fronts on atmospheric frontogenesis. *Journal of the Atmospheric Sciences*, 78(6), 1753–1771. <https://doi.org/10.1175/JAS-D-20-0118.1>
- Reichl, B. G., Hara, T., & Ginis, I. (2014). Sea state dependence of the wind stress over the ocean under hurricane winds. *Journal of Geophysical Research: Oceans*, 119(1), 30–51. <https://doi.org/10.1002/2013JC009289>
- Renard, R. J., & Clarke, L. C. (1965). Experiments in numerical objective frontal analysis. *Monthly Weather Review*, 93(9), 547–556. [https://doi.org/10.1175/1520-0493\(1965\)093<547:EINOFA>2.3.CO;2](https://doi.org/10.1175/1520-0493(1965)093<547:EINOFA>2.3.CO;2)
- Sauvage, C., Seo, H., Clayson, C. A., & Edson, J. B. (2023). Improving wave-based Air-Sea momentum flux parameterization in mixed seas. *Journal of Geophysical Research: Oceans*, 128(3), e2022JC019277. <https://doi.org/10.1029/2022JC019277>
- Seo, H., Miller, A. J., & Norris, J. R. (2016). Eddy–wind interaction in the California current system: Dynamics and impacts. *Journal of Physical Oceanography*, 46(2), 439–459. <https://doi.org/10.1175/JPO-D-15-0086.1>
- Seo, H., Miller, A. J., & Roads, J. O. (2007). The Scripps Coupled Ocean–Atmosphere Regional (SCOAR) model, with applications in the eastern Pacific sector. *Journal of Climate*, 20(3), 381–402. <https://doi.org/10.1175/JCLI4016.1>
- Seo, H., O'Neill, L. W., Bourassa, M. A., Czaja, A., Drushka, K., Edson, J. B., et al. (2023). Ocean mesoscale and frontal-scale Ocean–atmosphere interactions and influence on large-scale climate: A review. *Journal of Climate*, 36(7), 1981–2013. <https://doi.org/10.1175/JCLI-D-21-0982.1>
- Seo, H., Song, H., O'Neill, L. W., Mazloff, M. R., & Cornuelle, B. D. (2021). Impacts of ocean currents on the South Indian Ocean extratropical storm track through the relative wind effect. *Journal of Climate*, 1–61. <https://doi.org/10.1175/JCLI-D-21-0142.1>
- Seo, H., Subramanian, A. C., Miller, A. J., & Cavanaugh, N. R. (2014). Coupled impacts of the diurnal cycle of sea surface temperature on the Madden-Julian Oscillation. *Journal of Climate*, 27(22), 8422–8443. <https://doi.org/10.1175/JCLI-D-14-00141.1>
- Shchepetkin, A. F., & McWilliams, J. C. (2005). The regional oceanic modeling system (ROMS): A split-explicit, free-surface, topography-following-coordinate oceanic model. *Ocean Modelling*, 9(4), 347–404. <https://doi.org/10.1016/j.ocemod.2004.08.002>

- Shin, H. H., Hong, S.-Y., & Dudhia, J. (2012). Impacts of the lowest model level height on the performance of planetary boundary layer parameterizations. *Monthly Weather Review*, 140(2), 664–682. <https://doi.org/10.1175/MWR-D-11-00027.1>
- Skamarock, C., Klemp, B., Dudhia, J., Gill, O., Liu, Z., Berner, J., et al. (2019). A description of the advanced research WRF model version 4.1 (No. NCAR/TN-556+STR). <https://doi.org/10.5065/1dfh-6p97>
- Soster, F., & Parfitt, R. (2022). On objective identification of atmospheric fronts and frontal precipitation in reanalysis datasets. *Journal of Climate*, 35(14), 4513–4534. <https://doi.org/10.1175/JCLI-D-21-0596.1>
- Steffen, J., Seo, H., Clayton, C. A., Pei, S., & Shinoda, T. (2023). Impacts of tidal mixing on diurnal and intraseasonal air-sea interactions in the Maritime Continent. *Deep Sea Research Part II: Topical Studies in Oceanography*, 212, 105343. <https://doi.org/10.1016/j.dsr2.2023.105343>
- Stopa, J. E., Ardhuijn, F., Babanin, A., & Zieger, S. (2016). Comparison and validation of physical wave parameterizations in spectral wave models. *Ocean Modelling*, 103, 2–17. <https://doi.org/10.1016/j.ocemod.2015.09.003>
- Sullivan, P. P., Edson, J. B., Hristov, T., & McWilliams, J. C. (2008). Large-eddy simulations and observations of atmospheric marine boundary layers above nonequilibrium surface waves. *Journal of the Atmospheric Sciences*, 65(4), 1225–1245. <https://doi.org/10.1175/2007JAS2427.1>
- The WAVEWATCH III Development Group, W. (2019). *User manual and system documentation of WAVEWATCH III R © version 6.07 (Tech. Note 333)*. NOAA/NWS/NCEP/MMAB.
- Tolman, H. L., Balasubramanyan, B., Burroughs, L. D., Chalikov, D. V., Chao, Y. Y., Chen, H. S., & Gerald, V. M. (2002). Development and implementation of wind-generated ocean surface wave models at NCEP. *Weather and Forecasting*, 17(2), 311–333. [https://doi.org/10.1175/1520-0434\(2002\)017<0311:DAIOWG>2.0.CO;2](https://doi.org/10.1175/1520-0434(2002)017<0311:DAIOWG>2.0.CO;2)
- Trowbridge, J., Weller, R., Kelley, D., Dever, E., Plueddemann, A., Barth, J. A., & Kawka, O. (2019). The ocean observatories initiative. *Frontiers in Marine Science*, 6. <https://doi.org/10.3389/fmars.2019.00074>
- Warner, J. C., Sherwood, C. R., Arango, H. G., & Signell, R. P. (2005). Performance of four turbulence closure models implemented using a generic length scale method. *Ocean Modelling*, 8(1), 81–113. <https://doi.org/10.1016/j.ocemod.2003.12.003>
- Zheng, Y., Alapaty, K., Herwehe, J. A., Genio, A. D. D., & Niyogi, D. (2016). Improving high-resolution weather forecasts using the weather research and forecasting (WRF) model with an updated Kain–Fritsch scheme. *Monthly Weather Review*, 144(3), 833–860. <https://doi.org/10.1175/MWR-D-15-0005.1>
- Zhou, X., Hara, T., Ginis, I., D'Asaro, E., Hsu, J.-Y., & Reichl, B. G. (2022). Drag coefficient and its sea state dependence under tropical cyclones. *Journal of Physical Oceanography*, 52(7), 1447–1470. <https://doi.org/10.1175/JPO-D-21-0246.1>